BIOCHEMISTRY
including biophysical chemistry & molecular biology
Article

Biochemistry **2011,** *50,* 1875–1884 1875
DOI: 10.1021/bi101863g

Slow Conformational Dynamics in the Cystoviral RNA-Directed RNA Polymerase P2: Influence of Substrate Nucleotides and Template RNA†

Zhen Ren and Ranajeet Ghose*

The Graduate Program in Biochemistry, Graduate Center of the City University of New York, New York, New York 10016, United States, and Department of Chemistry, The City College of New York, New York, New York 10031, United States

Received November 22, 2010; Revised Manuscript Received January 10, 2011

ABSTRACT: The RNA-directed RNA polymerase P2 from cystovirus ϕ6 catalyzes the *de novo* synthesis of positive and negative strands of the viral double-stranded RNA genome. P2 is mobile on the slow, microsecond to millisecond time scale with various motional modes, putatively assisting in RNA translocation and catalysis. Here we investigate the influence of the extreme 3′-end sequence of the single-stranded RNA templates and the nature of the substrate nucleotide triphosphates on these motional modes using multiple-quantum NMR spectroscopy. We find that P2, in the presence of templates bearing the proper genomic 3′-ends or the preferred initiation nucleotide, displays unique dynamic signatures that are different from those in the presence of nonphysiological templates or substrates. This suggests that dynamics may play a role in the fidelity of recognition of the correct substrates and template sequences to initiate RNA polymerization.

The 75 kDa RNA-directed RNA polymerase (RdRP)[1] P2 from bacteriophage ϕ6 lies at the heart of the four-protein polymerase complex (PX) (*1*). The PX encloses the three-segment [small (S), medium (M), and large (L)] double-stranded RNA (dsRNA) genome and functions as the infectious particle in the host cytoplasm. P2 has an overall fold (see Figure 1) common to DNA and RNA polymerases and consists of fingers, palm and thumb domains (*2*, *3*) with additional loops (fingertips) connecting the fingers and the thumb forming an enclosed template tunnel that accommodates single-stranded but not double-stranded RNA (*4*). P2 contains the conserved polymerase sequence motifs A−F (*3*) and acts both as a replicase, synthesizing minus-strand RNA from plus-strand templates, and as a transcriptase, generating plus-strand RNA using minus-strand templates (*5*−*8*).

Several structures of P2, representing complexes with nucleotide triphosphate (NTP) substrates and single-stranded RNA (ssRNA) templates, are available (*4*, *9*−*11*). These structures provide detailed insight into the nature of the initiation complex, template requirement, and metal ion specificity. In spite of the availability of a large amount of crystallographic information, a substantial degree of conformational dynamics is required (as discussed below) to interpret these static snapshots in mechanistic and functional terms (*4*). For RdRPs such as the poliovirus 3Dpol for which both structural and kinetic data are available (*12*), the need for significant conformational rearrangements to reconcile structural and biochemical information is evident. For example, as revealed by biochemical studies, a basic residue (Lys359) on highly dynamic motif D functions as a general acid protonating the pyrophosphate product (*13*). However, this residue has not been crystallographically trapped in a conformation consistent with this role (*14*). Indeed, the rate-limiting step for phosphodiester bond formation has been suggested to be a conformational change (*12*, *15*). In addition, a large amount of evidence hinting that catalysis by RNA polymerases may be influenced by effects transmitted from distant sites exists, e.g., a remote site that has been shown to exert allosteric control over transcriptional fidelity in 3Dpol (*16*, *17*). Similar effects have also been seen in a close structural homologue of P2, hepatitis C virus polymerase (HCVpol). HCVpol contains a surface GTP-binding site that though distant (~30 Å) from the catalytic center can be targeted by small molecule inhibitors of catalytic activity (*18*).

Given these indications suggesting a role played by dynamics in RNA polymerase function (*14*), the need to characterize these effects in representative RNA polymerases in atomistic detail at specific steps along the catalytic pathway to complement available structural and biochemical information cannot be overstated. With this goal in mind, we recently characterized dynamics of ϕ6 P2 on the fast (picoseconds to nanoseconds) and slow (microseconds to milliseconds) time scales using the 25 Ile residues, which are more-or-less evenly distributed over its structural domains and conserved sequence motifs, as probes (*19*). We found that, for apo P2, on the fast time scale, the entrances to both the template and substrate entry portals (see Figure 1) were highly dynamic; the catalytic motifs were rigid, becoming more ordered in the presence of ssRNA. More importantly, on the slow time scale considered to be relevant for catalysis, two broadly classified dynamic regimes (Figure 1 and Table 1) were seen represented: a faster time scale (group I with an effective rate constant k_{ex} of

†This work is supported by National Science Foundation Grant MCB0843141 and National Institutes of Health Grant 5G12 RR03060 (partial support of the NMR facilities at The City College of New York).

*To whom correspondence should be addressed. E-mail: rghose@sci.ccny.cuny.edu. Phone: (212) 650-6049. Fax: (212) 650-6107.

[1]Abbreviations: AMPCPP, adenosine 5′-[(α,β)-methyleno]-triphosphate; CPMG, Carr−Purcell−Meiboom−Gill; CTD, C-terminal domain; dsRNA, double-stranded RNA; GMPCPP, guanosine 5′-[(α,β)-methyleno]triphosphate; HMQC, heteronuclear multiple-quantum correlation; MQ, multiple-quantum; PX, polymerase complex; SQ, single-quantum; ssRNA, single-stranded RNA; RF, radio-frequency; RdRP, RNA-directed RNA polymerase.

Published on Web 01/18/2011

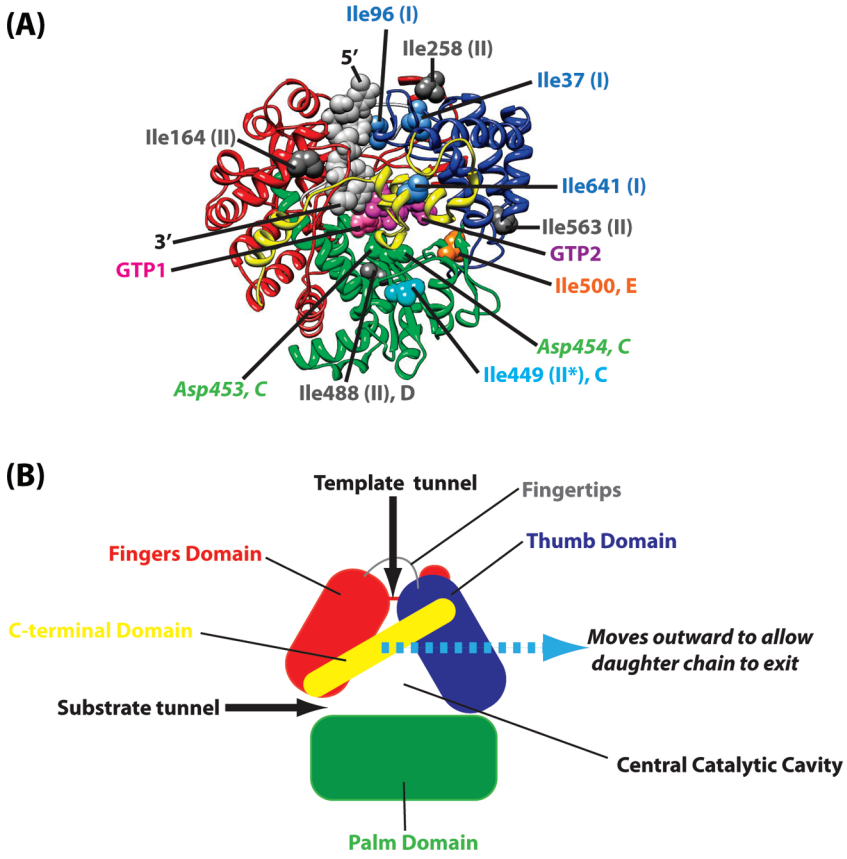

FIGURE 1: (A) ϕ6 P2 showing the conserved polymerase fold (*4*). The fingers domain (red; residues 1−30, 104−276, and 333−397), thumb domain (blue; residues 37−91 and 518−600), palm domain (green; residues 277−332 and 398−517), and C-terminal domain (yellow; residues 601−664) are shown. Key Ile residues that are shown to undergo slow, microsecond to millisecond time scale dynamics in apo-P2 characterized previously (*19*) are labeled. Ile residues that belong to group I and group II are represented by blue and dark gray spheres, respectively, and labeled accordingly. Ile449 (motif C) undergoes slow dynamics (group II) under only certain circumstances (denoted with an asterisk) and is depicted as a light blue sphere. Ile500 (motif E) that switches between the fast (group I) and slow motional (group II) modes is colored orange. The two bound GTP molecules (pink and purple) are shown, as is the template single-stranded RNA (gray, 5′- and 3′-ends labeled). The conserved Asp residues, Asp453 and Asp454 (a part of the G/SDD motif found in DNA and RNA polymerases), that lie on motif C are represented as green spheres and labeled. (B) Schematic representation of the P2 structure showing the structural domains and template and substrate channels.

Table 1: Residues That Exhibit Slow Microsecond to Millisecond Time Scale Dynamics[a]

residue	location	slow motional time scale
Ile37	thumb, template entry portal	I
Ile96	fingertips, template entry portal	I
Ile164[b]	fingers, plough region	II
Ile258	fingers	II
Ile449[c]	palm, motif C	II
Ile488	palm, motif D	II
Ile500	palm, motif E	switches between I and II
Ile563	base of thumb	II
Ile641[d]	C-terminal domain	I

[a]These are the motional time scales seen for most of the states analyzed (*19*). [b]The plough region is known to be coupled to transcriptional efficiency, i.e., catalysis (*11*). [c]Motif C bears the conserved ^{452}S-(G)DD^{454} motif. [d]The motion of the C-terminal domain seems to assist in the exit of the daughter chain (*4*).

~1200−1500 s^{-1}) and a slower time scale (group II with a k_{ex} of ~500−800 s^{-1}) (*19*). The group I motional time scale, involving the template entry portal (probed by Ile37 and Ile96) and the C-terminal domain (CTD, probed by Ile641), was coincident with that predicted for template translocation from kinetic analyses of RNA (*12*) and DNA (*15*) polymerases. Indeed, their locale was in line with current models for template translocation by motions of the thumb and the fingertips (*20*) and exit of the daughter chain by motion of the CTD (*4*). However, motions that involve RNA translocation have been shown not to be rate-limiting in DNA (*15*) and RNA (*12*) polymerases.

An analysis of the nucleotide addition cycle in the homologous RNA polymerase 3Dpol used three kinetic processes to model the slow steps of the nucleotide addition cycle. (1) The ternary complex of polymerase, RNA, and substrate nucleotides undergoes a conformational change to form an activated complex ($k_{forward}$ = 300 s^{-1}, and $k_{reverse}$ = 500 s^{-1}; expected k_{ex} in dispersion experiments of 800 s^{-1}). (2) Single-nucleotide addition occurs through formation of a new phosphodiester bond between two substrate nucleotides ($k_{forward}$ = 520 s^{-1}, and $k_{reverse}$ = 375 s^{-1}; expected k_{ex} in dispersion experiments of 895 s^{-1}). (3) Deactivation of the product complex (with the product pyrophosphate bound) occurs ($k_{forward}$ = 500 s^{-1}, and $k_{forward} \gg k_{reverse}$; expected k_{ex} in dispersion experiments of ~500 s^{-1}) (*12*). These steps are followed by faster pyrophosphate release and RNA translocation. While similar measurements are not available for P2, the overall similarities between 3Dpol and P2 would suggest that similar functional mechanisms and rates could be expected for the nucleotide addition cycle of P2. This puts the k_{ex} values relevant to catalysis in the same time regime as those seen for the slower, group II

motions (*19*). Therefore, we sometimes refer to group II motions as those occurring on the "catalytic time scale", suggesting only a coincidence of dynamic rates determined by NMR with those proposed to be relevant for catalysis. These group II motions were reported for Ile residues (Table 1) near the catalytic site (Ile449 on motif C and Ile488 on motif D), at remote sites shown to be coupled to transcriptional efficiency (Ile164 in the "plough" region) (*11*), and at additional residues located on the outer edge of the template tunnel (Ile258 on the fingers) and Ile563 (on the base of the thumb). In addition, Ile500 that lies on motif E (palm) seemed to switch between time scales I and II depending on the complexes analyzed, representing different points along the catalytic pathway. That work (*19*) represented the first instance of a comprehensive analysis of the dynamics of a full-length canonical RdRP by NMR. Recently, Yang et al. (*17*) utilized a similar coarse-grained approach, using the 17 Met residues in 3Dpol to demonstrate very long range effects on catalytic fidelity by NMR relaxation measurements in solution.

To obtain further insight into the role of motion in P2 function, here we analyze the conformational dynamics of P2 using relaxation dispersion measurements of $^{13}C-^{1}H$ multiple-quantum coherences (*21*) at the 25 Ile $\delta1$ positions in P2, focusing specifically on the influence of the substrate NTPs, and the sequence of the template ssRNA, thereon. Thus, combining results from our previous publication (*19*) with new data obtained for P2 in the presence of a set of template ssRNAs, an additional NTP substrate, and a nonphysiological initiation complex (to contrast its differences with a correct physiological one), we find additional support for the notion that dynamics may indeed play a role in RNA processing by P2. Our results indicate that the nature of dynamics in P2 in the presence of the physiologically correct substrates and ssRNA templates is distinct from that in the presence of nonoptimal substrates and nongenomic template sequences.

MATERIALS AND METHODS

Expression, Purification, Sample Preparation, and Resonance Assignment of ϕ6 P2. The detailed protocol for expression and purification of ϕ6 P2 has been described in depth in our recent paper (*19*) and is not reproduced here. In brief, the ϕ6 P2 plasmid was constructed from the pLM687 plasmid as described previously (*22*) and subcloned into a pET28a(+) (Strategene) vector between the NdeI and EcoRI sites. The P2 protein was expressed as an N-terminal His_6 fusion using *Escherichia coli* BL21-DE3 (Agilent) cells preadapted for growth in D_2O using M9 medium prepared in 100% D_2O containing 3 g/L [U-^{12}C,^{2}H]glucose and 1 g/L $^{15}NH_4Cl$ as the sole carbon and nitrogen sources, respectively, followed by addition of 50 mg of 2-keto-3-d_2-4-[^{13}C]butyrate (Cambridge Isotope Laboratories) at an OD_{600} of 0.6 and induction using 1 mM IPTG after growth for 1 h. The uniformly ^{15}N,^{2}H-Ile-$\delta1$-^{13}C,^{1}H-labeled P2 protein was purified using nickel affinity (Ni-NTA agarose, Qiagen) chromatography and exchanged into a buffer containing 20 mM bis-tris, 400 mM NaCl, 4 mM DTT, and 5 mM $MgCl_2$ (pH 6.5). This buffer was taken to be the reference state in determining chemical shift perturbations and in the relaxation dispersion experiments. Note that this corresponds to the Mg^{2+}-bound state described by Ren et al. (*19*). The P2 concentration in the NMR experiments varied from 250 to 300 μM.

Spectral Analyses. All NMR experiments were performed at 25 °C on a Varian Inova 600 MHz spectrometer equipped with a triple-resonance {^{1}H,^{13}C} cryogenic probe capable of applying pulsed field gradients along the *z*-axis. Sweep widths of 9000 and 1600 Hz in the direct (^{1}H, 512 complex points) and indirect (^{13}C, 32 complex points) dimensions, respectively, were used for all NMR experiments. The ^{13}C carrier was positioned at 13.15 ppm (the center of the Ile ^{13}C $\delta1$ resonances for P2).

The $^{13}C-^{1}H$ resonances corresponding to the $\delta1$ positions of the 25 Ile residues in ϕ6 P2 were assigned using a combination of 13 single and 12 triple Ile → Leu mutants using a strategy that has been described in detail previously (*19*). Resonances corresponding to Ile211 and Ile283 could not be assigned with confidence, and therefore, chemical shift perturbations and relaxation dispersion data corresponding to these resonances were not analyzed.

Chemical shift changes (with respect to the reference state, $\Delta\delta$ in hertz) in the presence of template ssRNA or substrate NTPs or in the ternary complexes were calculated using

$$\Delta\delta = \nu_0\sqrt{(\delta_{\mathrm{ref,H}}-\delta_{\mathrm{H}})^2+\left[\frac{\gamma_{\mathrm{C}}}{\gamma_{\mathrm{H}}}(\delta_{\mathrm{ref,C}}-\delta_{\mathrm{C}})\right]^2} \quad (1)$$

where $\delta_{\mathrm{ref,C}}$ and $\delta_{\mathrm{ref,H}}$; δ_{C} and δ_{H}, are the ^{13}C and ^{1}H chemical shifts (in $^{13}C-^{1}H$ HMQC spectra) in the reference state and particular complexes, respectively. The spectrometer frequency ν_0 was 600 MHz. AMPCPP (purchased from Sigma) and GMPCPP (custom synthesized by Jena Biosciences), the nonhydrolyzable analogues of the substrates ATP and GTP, respectively, were obtained commercially. The AMPCPP and GMPCPP concentrations were kept at 5 mM in all states that required their use. ssRNA constructs for the NMR studies were purchased as PAGE-purified species from Integrated DNA Technologies Inc. The ssRNA concentration in NMR experiments was kept at least 5 times that of P2. All NMR samples contained 1 unit of an RNase inhibitor (New England Biolabs) per microliter.

Fluorescence Anisotropy Measurements. Fluorescence anisotropy measurements were performed using ssRNA oligos labeled at the 5′-end with 6-carboxyfluorescein. The HPLC-purified oligos were purchased from Dharmacon RNAi Technologies. All experiments utilized a Panvera Beacon 2000 fluorescence anisotropy system with excitation at 490 nm and analysis of the emitted fluorescence after it had passed through a 520 nm cutoff filter. Four combinations of the horizontal and vertical polarization filters were used with a 10 s averaging time. The measured intensities for the four polarizer settings in the presence of increasing amounts of P2 were converted into anisotropy (A) values, and the dissociation constants (K_{d}) were obtained from the following equation:

$$A(C)-A(0) = [A_\infty - A(0)] \times \frac{K_{\mathrm{d}}+C_{\mathrm{RNA}}+C-\sqrt{(K_{\mathrm{d}}+C_{\mathrm{RNA}}+C)^2-4C_{\mathrm{RNA}}C}}{2C_{\mathrm{RNA}}} \quad (2)$$

where $A(C)$ is the anisotropy when the concentration of P2 equals C and A_∞ is the limiting anisotropy value. The concentration of RNA (C_{RNA}) was kept constant at 5 nM. All experiments were performed at pH 6.5 in NMR buffer containing 1 unit of RNase inhibitor (New England Biolabs) per microliter. The reduced absolute fluorescence of the carboxyfluorescein moiety at this pH

does not lead to any complications as demonstrated previously (*19*).

All fits to experimental data (eqs 2 and 4) were performed using in-house programs that utilize the ODRPACK subroutines (*23*). Errors in the fitted parameters were obtained from the inverse covariance matrices of the fits and included both random and model selection errors.

Multiple-Quantum Dispersion Measurements. $^{13}C-^{1}H$ multiple-quantum relaxation dispersion curves were obtained using pulse sequences developed by Korzhnev et al. (*21*). Fifteen values of the RF field strength ($\nu_1 = {}^1/_2\tau_{CPMG}$, where τ_{CPMG} is the spacing between successive π pulses) (31.25, 62.5, 93.75, 125.0, 156.25, 187.5, 250.0, 312.5, 375.0, 437.5, 500.0, 625.0, 750.0, 875.0, and 1000 Hz) were used with a constant relaxation delay of 32 ms, collecting 128 transients per t_1 point. Data for each ν_1 value were acquired in an interleaved fashion, with all ν_1 values collected prior to t_1 incrementation to minimize possible errors resulting from sample heating and/or precipitation and to increase the accuracy of the fitted exchange parameters. The peak intensities [$I(\nu_1)$], and errors thereof, for each of the resonances corresponding to the 25 Ile residues were obtained by a nonlinear least-squares analysis of the two-dimensional line shapes for spectra recorded for each value of ν_1. The reference spectrum used for peak picking was missing the relaxation delay ($T = 0$) and was collected in triplicate to assess spectrometer and sample stability. The two-dimensional least-squares fits were conducted using the nlinLS module of the NMRpipe software package (*24*). The measured intensities $I(\nu_1)$ were converted into effective multiple-quantum relaxation rates [$\Gamma_{MQ,eff}(\nu_1)$] using the following formula:

$$\Gamma_{MQ,eff}(\nu_1) = -\frac{1}{T}\ln\frac{I(\nu_1)}{I_0} \quad (3)$$

where I_0 is the peak intensity averaged over the three measurements of the reference spectrum. The errors in $\Gamma_{MQ,eff}(\nu_1)$ were obtained by using standard error propagation (for eq 3) utilizing the errors in I_0 and $I(\nu_1)$ from the nonlinear least-squares analysis of the two-dimensional line shapes.

All dispersion data were fitted assuming the fast exchange regime (see below) using eq 4 (*21*, *25*). The $\Gamma_{MQ,eff}(\nu_1)$ values in this regime are given by

$$\Gamma_{MQ,eff}(\nu_1) = \Gamma_{MQ}(\infty) + \frac{\xi}{k_{ex}}\left[1 - \frac{4\nu_1}{k_{ex}}\tanh\left(\frac{k_{ex}}{4\nu_1}\right)\right] \quad (4)$$

where k_{ex} is the sum of the forward and reverse rates assuming a two-state exchange model ($A \rightleftarrows B$), $\xi = 2p_A(1 - p_A)\Delta\omega_H\Delta\omega_C$, p_A is the fractional occupancy of state A (the fractional occupancy of state B, p_B, equals $1 - p_A$), and $\Gamma_{MQ}(\infty)$ is the limiting value of the MQ relaxation rate, i.e., the value of $\Gamma_{MQ,eff}$ in the absence of chemical exchange. The condition of a small $\Delta\omega_H\Delta\omega_C$ in addition to the fast exchange regime where $(\Delta\omega_H\Delta\omega_C)^{1/2} \ll k_{ex}$, is required for eq 4 to hold (*19*). In our case, this is expected to be valid even for states that involve tighter binding because we are not directly probing the specific residues directly involved in the binding process, a fact borne out by the relatively small chemical shift perturbations seen. The approach utilized here allows only the k_{ex} values, obtained as one of the parameters in a three-parameter [k_{ex}, $\Gamma_{MQ}(\infty)$, and ξ] fit of the experimental dispersion curves to eq 4, to be interpreted quantitatively.

Table 2: Apparent Binding Affinities of ϕ6 P2 for Single-Stranded RNA Sequences[a]

template	sequence	K_d (μM)
C1	5′-UUU<u>CC</u>-3′[b]	53.2 ± 3.5[e]
C2	5′-UUU<u>AC</u>-3′[c]	295.9 ± 15.2
C3	5′-UUU<u>CU</u>-3′[d]	15.3 ± 1.4
C4	5′-UUU<u>UC</u>-3′	6.6 ± 0.4[e]
C5	5′-UUU<u>UU</u>-3′	1.2 ± 0.1
C6	5′-UUUUU<u>CC</u>-3′[b]	129.9 ± 4.4
C7	5′-UUUUU<u>CU</u>-3′[d]	15.0 ± 0.7

[a]Relaxation data were collected for P2 in the presence of templates that are indicated in boldface (see Table 3). [b]The 3′-end of the minus strands of the M (m^-) and S (s^-) genomic segments. [c]The 3′-end of the minus strands of the L (l^-) genomic segment. [d]The 3′-end of the plus strands of the L (l^+), M (m^+), and S (s^+) genomic segments. [e]In agreement with that reported by Ren et al. (*19*).

In almost all of the cases, data for all 15 ν_1 values were used in the individual fits. In a small number of cases, one or two data points for which the errors in the $I(\nu_1)$ values were more than 50% (resulting from a low signal-to-noise ratio) greater than the average error for all points in that series were excluded from the final fits. The points that fulfilled this criterion were Ile500 for the reference state (two points) and Ile449 for TC_A (two points) (as explicitly stated in Tables 3−5), as determined with data collected for our previous publication (*19*). The new k_{ex} values obtained in these cases were unchanged within error bounds.

In additional to the individual fits, we also performed global fits for residues that displayed the fast (group I) and slow (group II) dynamic modes. This was accomplished by using a grid search over the k_{ex} values (a common value was used for all residues within the group) combined with an orthogonal distance regression for individual $\Gamma_{MQ}(\infty)$ and ξ values (eq 4). The boundaries of the grid space were defined by the upper and lower bounds of the k_{ex} values obtained by the fits of individual residues in the group and adjusted if required. A grid size of 50 s^{-1} was used. The level of theory and experimental precision used here cannot justify use of a finer grid.

Another point to note is that the exchange processes determined here arise from true conformational dynamics given that the ligand binding and unbinding, i.e., on and off processes, respectively, are expected to be at least 2 orders of magnitude faster (for the highest K_d value) than the fastest rate measured here, assuming a diffusion-controlled on rate. Therefore, these on and off processes are unlikely to contribute to the k_{ex} values obtained in this case.

RESULTS AND DISCUSSION

Influence of Template 3′-Ends. It has been shown that for ϕ6 P2, the efficiency of RNA polymerization depends on the sequence at the extreme 3′-ends of the ssRNA template, especially with respect to the two penultimate bases (*6*, *8*). The 3′-ends of the minus strands of the S (s^-) and M (m^-) genomic segments that contain a 5′-...UUU<u>CC</u>-3′ sequence are utilized more efficiently than the minus strand of the L segment (l^-) that contains a 5′-...UUU<u>**AC**</u>-3′ sequence or the 3′-ends of the genomic plus strands (s^+, m^+, l^+) containing a 5′-...UCU<u>**CU**</u>-3′ sequence. We first tested whether this difference in template utilization could be attributed to the affinity with which P2 recognizes the 3′-end sequence. We measured the affinities toward P2 of five five-nucleotide templates [C1−C5 (see Table 2)] with varying 3′-end sequences, by

monitoring the change in the fluorescence anisotropy of these constructs bearing a 5′-carboxyfluorescein tag in the presence of increasing amounts of protein. The affinities of two additional seven-nucleotide templates were also measured (Table 2). The K_d values (Table 2) thus obtained varied from 1.2 ± 0.1 μM (C5) to 295.9 ± 15.2 μM (C2), with those corresponding to the 3′-segments of the genomic minus strands (C1 and C6, s^- and m^-; C2, l^-) binding with the lowest affinity

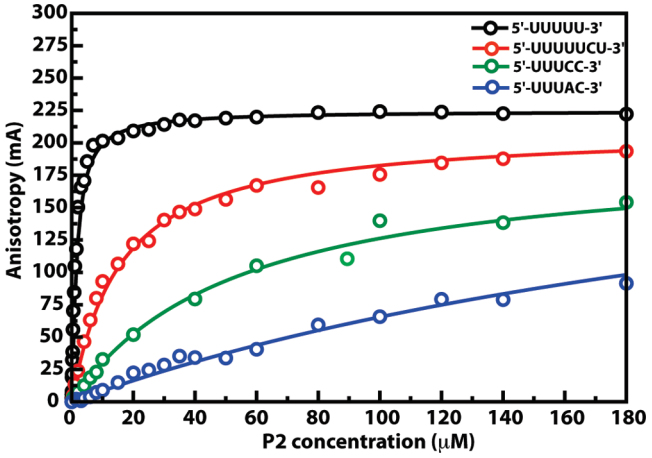

FIGURE 2: Representative binding curves demonstrating the affinities of several ssRNA constructs for ϕ6 P2, determined by fluorescence anisotropy measurements using 5′-carboxyfluorescein-tagged ssRNA. Only a few binding curves are shown for ease in illustrating their differences.

(Figure 2). On the basis of our analysis, it appears that P2 prefers U over C at the 3′-ends for stronger binding. The greatly reduced affinity for the sequence corresponding to the 3′-end of l^- (C2) may be explained by the presence of a larger purine base (A), as previously suggested (*4*). Interestingly, sequences containing a UU (C5) or a CU (as in the genomic s^+, m^+, and l^+; C3 and C7) at their 3′-ends have a substantially higher affinity for P2 but are processed less efficiently compared to the CC sequence (as in s^- and m^-; C1 and C6). Thus, the affinity follows this trend (strongest to weakest binding): UU > UC > CU > CC > AC. The template efficiency follows this trend: CC > UC > AC > CU (*6*, *8*). It is also known that templates bearing a UU at the 3′-end are less efficiently utilized than those terminated with a UC sequence (*6*). Thus, template utilization and by inference formation of a stable functional initiation complex cannot be related in a simple way to binding affinity and is likely a more complex function of affinity and changes in structure and dynamics of P2 resulting from template and substrate binding.

Next, we tested whether the nature of ssRNA sequence plays a role in modifying the dynamics of P2 on the slow, microsecond to millisecond time scale by measuring the RF field (ν_1) dependence of the Ile Cδ1 $^{13}C-^1H$ MQ relaxation rates. We collected data for three constructs (C1, C2, and C5) that span the range of K_d values (Table 2), with the first representing the genomic s^- and m^- 3′-ends and the second the 3′-end of the genomic l^- segment, the two weakest binders, and the third (C5) being the strongest binder to P2. Representative examples of experimental dispersion curves and the corresponding fits to eq 4 are depicted in Figure 3. An

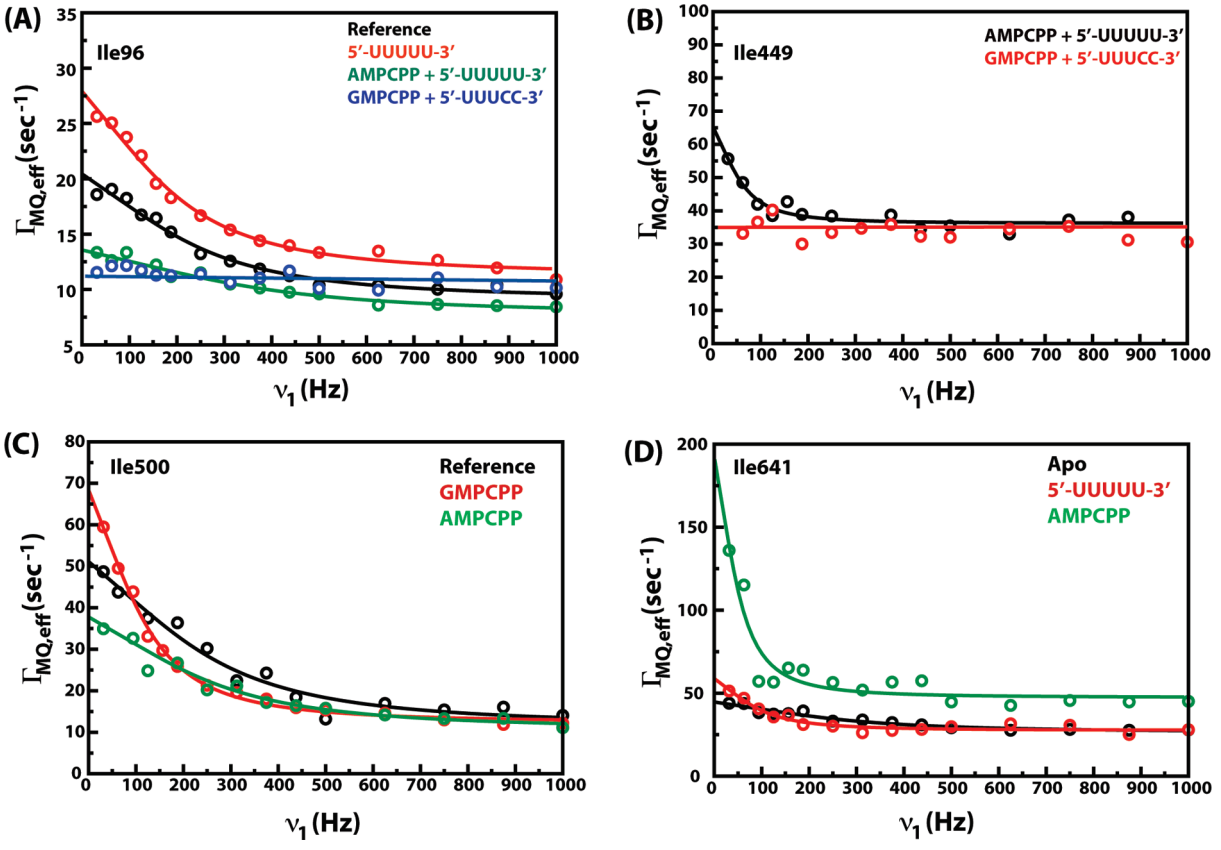

FIGURE 3: Representative dispersion curves with experimental data depicted by circles and fits to eq 4 by solid lines. (A) Data for fingertip domain residue Ile96. (B) Data for motif C residue Ile449. (C) Data for motif E residue Ile500. (D) Data for Ile641 that lies in the C-terminal domain. The blue line in panel A and the red line in panel B are drawn to guide the eye and do not represent fits. These correspond to situations in which the dispersion curves are flat; i.e., $\Gamma_{MQ,eff}$ values are independent of ν_1. Data for only a small number of states are shown for the sake of clarity.

overlay of $^{13}C-^{1}H$ HMQC spectra of P2 in the presence of the three constructs is shown in Figure 4 to illustrate the spectral quality.

The common feature of the influence on the slow dynamics of P2 for the three ssRNAs tested (Table 3) was the complete suppression of slow motion in the group II residue Ile563 that lies at the base of the thumb domain (Figure 1). However, the correct genomic 3′-ends (C1 and C2) also resulted in a complete suppression of slow dynamics in the group II Ile258 (on the fingers domain), while this motion persisted for C5. Ile641 that has been shown to be dynamic on the group I time scale [quantitative data could not be obtained for this residue in the reference state; a k_{ex} value of $1358 \pm 109\ s^{-1}$ was found in the apo state (*19*)] seemed to display dynamics on a much slower time scale [$k_{ex} = 580 \pm 112\ s^{-1}$ (see Figure 3D)] in the presence of the nonphysiological template C5, suggesting a decoupling of the motions of the CTD and the edge of the template entry portal and the fingertips. In addition to these perturbations in dynamics, significant differences in chemical shift perturbations (Figure 5A) induced by the genomic constructs C1, C2, and C5 were seen. Notably, Ile641 exhibited comparable shift changes for C1 (47 Hz) and C2 (42 Hz), while the changes for C5 were much more modest (13 Hz). A marginally smaller chemical shift change was also seen in Ile164 for C5 (13 Hz) compared with C1 (19 Hz) and C2 (18 Hz). This suggests that the proper genomic 3′-ends elicit specific and unique changes in structure and dynamics compared with the nonphysiological (C5) template despite having 44-fold (C1) and 247-fold (C2) less affinity for P2. No significant differences in the dynamic time scales or chemical shifts were noted for any of the residues that lie near the catalytic site: Ile449 (motif C), Ile488 (motif D), and Ile500 (motif E).

Influence of Substrate Purine Nucleotide Triphosphates. Next we tested the influence of the substrate NTPs on slow dynamics in P2 (in the absence of RNA). The purine nucleotides GTP and ATP are required initially in $\phi 6$ given the pyrimidine-rich 3′-end of the genomic segments. Indeed, GTP is the preferred initiation nucleotide for $\phi 6$ and a host of other viral RNA polymerases that initiate RNA synthesis *de novo*, including those from bovine diarrhea virus (BVDV), HCV, broom mosaic virus (BMV), etc. (*26*). This is especially important because the exact order of substrate and RNA binding to P2 is not precisely known and prebinding of the initiation nucleotide (GTP) cannot be ruled out, as suggested by Choi et al. (*20*). For this study, we utilized AMPCPP and GMPCPP, the α,β nonhydrolyzable analogues of ATP and GTP, respectively, to allow complex formation but not catalysis in the ternary complexes discussed below. The overall differences in chemical shift changes induced were quite modest (Figure 5B), though some of the largest changes were

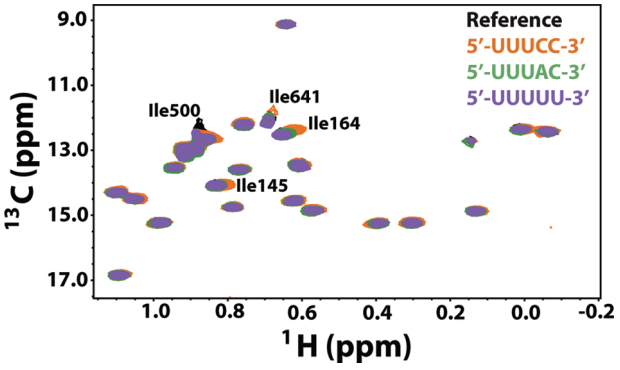

FIGURE 4: Overlay of the reference spectra [$\phi 6$ P2 in NMR buffer (black)] with each of three templates, C1 [5′-UUU**CC**-3′, 3′-ends of the genomic s^- and m^- strands (orange)], C2 [5′-UUU**AC**-3′, 3′-end of the genomic l^- (green)], and C5 [5′-UUU**UU**-3′ (purple)].

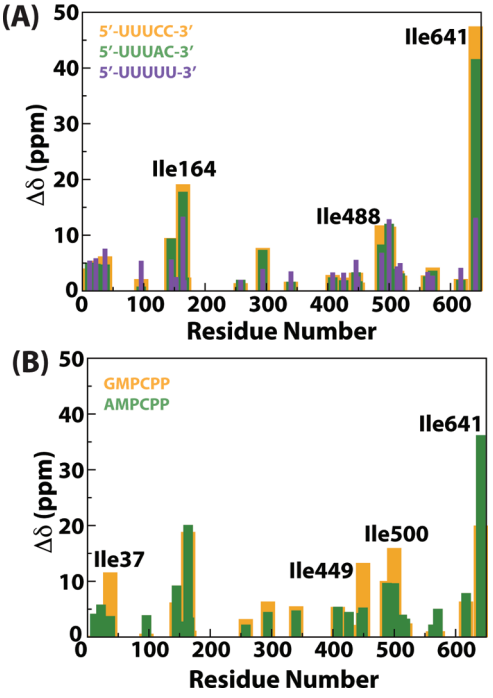

FIGURE 5: (A) Scaled chemical shift changes shown for each of the three templates, C1 (yellow), C2 (green), and C5 (purple), and the reference (black). (B) Scaled chemical shift changes for the substrate analogues [GMPCPP (yellow) and AMPCPP (green)]. Scaled chemical shift changes, with respect to the reference, for panels A and B were calculated using eq 1.

Table 3: k_{ex} Values (s^{-1}) of P2 in the Presence of Different Single-Stranded RNA Templates[a]

state	Ile37	Ile96	Ile164	Ile258	Ile488	Ile500	Ile563	Ile641
reference[b]	1292 ± 86	1537 ± 142	210 ± 109	311 ± 74	577 ± 61	1613 ± 232[c]	418 ± 241	X
C1	1535 ± 382	1132 ± 257	X	ND	491 ± 176	1450 ± 274	ND	X
C2	1140 ± 265	1007 ± 104	X	ND	547 ± 157	1193 ± 284	ND	X
C5	1145 ± 98	1287 ± 95	306 ± 116	734 ± 192	403 ± 174	1486 ± 248	ND	580 ± 112

[a]ND implies that the relaxation rate ($\Gamma_{MQ,eff}$) was independent of the applied ν_1 field. X implies that the quality of the data did not allow quantitative k_{ex} values to be extracted. Data for Ile449 are not shown here and in Table 4 because the states characterized do not show field-dependent relaxation rates (i.e., ND) or the quality of the data did not allow quantitative estimation of the k_{ex} values (i.e., X). [b]P2 in NMR buffer containing 5 mM Mg^{2+} was taken as the reference state. Data for the reference state are from ref *19*. [c]Data for Ile500 in the reference state were refitted excluding two points with large errors. The k_{ex} value obtained was unaltered within confidence bounds compared to that obtained previously (*19*).

Table 4: k_{ex} Values of P2 in the Presence of Substrate NTPs

state	Ile37	Ile96	Ile164	Ile258	Ile488	Ile500	Ile563	Ile641
reference[a]	1292 ± 86	1537 ± 142	210 ± 109	311 ± 74	577 ± 61	1613 ± 232[b]	418 ± 241	X
AMPCPP	1405 ± 140	3010 ± 679	ND	ND	343 ± 107	1634 ± 166	ND	336 ± 84
GMPCPP[a]	1214 ± 207	2105 ± 430	ND	ND	679 ± 93	767 ± 35	ND	X

[a]Reference and GMPCPP data from ref *19*. [b]Data for Ile500 in the reference state were refitted excluding two points with large errors. The k_{ex} value obtained was unaltered within confidence bounds from that obtained previously (*19*).

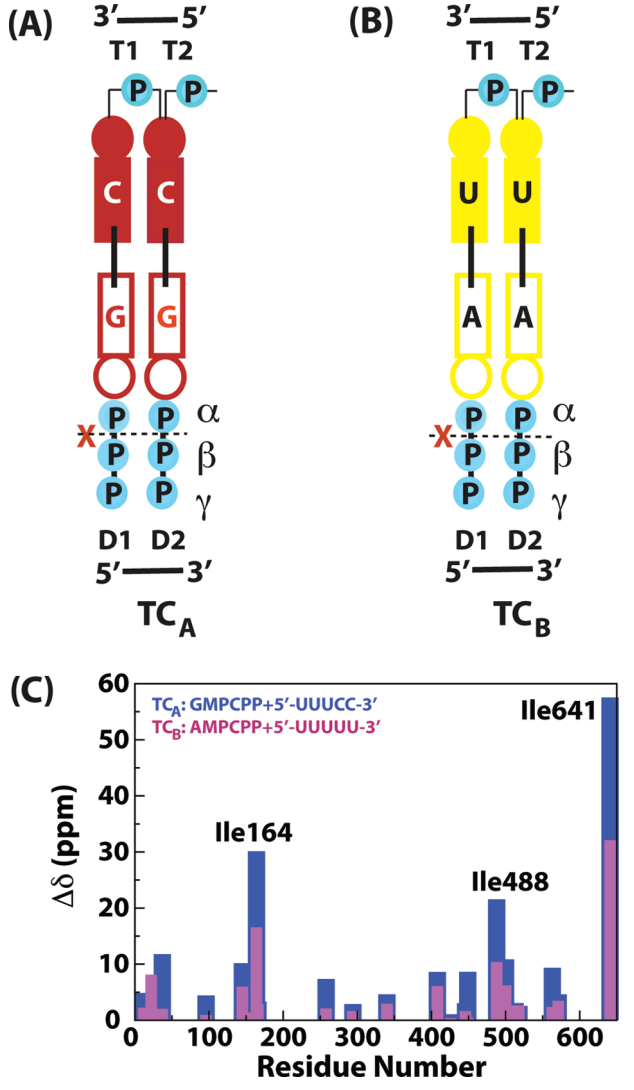

FIGURE 6: (A) TC_A is the ternary complex formed by 5′-UUU**CC**-3′ (template C1), the nonhydrolyzable GTP analogue GMPCPP, and ϕ6 P2. Template bases T1 and T2 (numbered from 3′ to 5′) base pair with substrate bases D1 and D2 (numbered from 5′ to 3′) forming a stable initiation complex (based on base-pairing considerations alone). The first phosphodiester bond forms between D1 and D2, creating the daughter chain and releasing pyrophosphate. In TC_A, D2 (and D1) is the substrate GMPCPP that cannot be hydrolyzed between the α- and β-phosphates and the reaction cannot proceed, though the initiation complex forms. TC_A is physiologically relevant because template 1 corresponds to the 3′-ends of the s^- and m^- genomic segments. (B) TC_B is the ternary complex formed by template C5 (5′-UUU**UU**-3′) and the nonhydrolyzable ATP analogue AMPCPP, and also allows proper base pairing between T1 and D1 and between T2 and D2, as in TC_A above. C5 does not correspond to 3′-ends of any of the ϕ6 genomic segments. (C) Scaled chemical shift changes (with respect to the reference state) shown for ternary complexes TC_A (blue) and TC_B (pink).

localized near the active site. Ile449 (motif C) and Ile500 (motif E) exhibited larger chemical shift changes for GMPCPP (13 and 16 Hz, respectively) than for AMPCPP (5 and 10 Hz, respectively), indicating larger conformational changes around the active site for the GTP analogue. In contrast, a much larger chemical shift change for Ile641 (CTD) was noted for AMPCPP (36 Hz) compared with GMPCPP (20 Hz).

Differences in dynamic time scales were more pronounced (summarized in Table 4). In the presence of GMPCPP, the motion of Ile500 on motif E changed from a faster time scale [group I (see Table 1)] in the reference state to a catalytic time scale [group II (Figure 3C)]. AMPCPP induced no such change. Additionally, for AMPCPP (as in the case of template C5 discussed above), the dynamics of Ile641 (CTD) seemed to shift toward a slower time scale (k_{ex} = 336 ± 84 s^{-1}) (Figure 3D) around the group II range rather than group I-type dynamics characteristic of this region (*19*) (Table 1). While the quality of the data for this residue in the presence of GMPCPP did not allow us to extract a quantitative k_{ex} value, a k_{ex} value of 1344 ± 110 s^{-1} (*19*) was found for this residue in the presence of GMPPNP, indicative of group I dynamics. Here too, as in C5 (above), the incorrect ligand leads to a decoupling of the motion of the template entry portal with the CTD.

Ternary Complexes. Finally, we analyzed two ternary complexes that should form stable initiation platforms on the basis of proper complementarity between template 3′-end sequence and substrate NTPs. These were TC_A {P2−GMPCPP−C1 [for which data are available from ref *19* (Figure 6A)]} and TC_B [P2−AMPCPP−C5 (Figure 6B)]. Significant differences in dynamics were noted between TC_A representing the initiation platform formed during the transcription of the genomic s^- and m^- strands and TC_B that is nonphysiological in the context of ϕ6. The most striking difference was the complete suppression of the slow dynamics of Ile96 (fingertips, at the template entry portal) in TC_A (Figure 3A and Table 5).

Near the catalytic site, the motion of Ile500 in TC_A (Figure 3C) seemed to be shifted slightly toward the catalytic time scale [k_{ex} = 972 ± 186 s^{-1} (Table 5)] from a faster time scale. However, the most significant difference between the two complexes was the detection of slow motion on a catalytic time scale for Ile449 [k_{ex} = 381 ± 95 s^{-1} (Table 5 and Figure 3B)] that lies on motif C (bearing Asp453 and Asp454 from the conserved DD motif) in TC_A but not in TC_B. These differences in dynamics between the physiological (TC_A) and nonphysiological (TC_B) complexes were also reflected in the chemical shifts. The chemical shift changes seen in TC_A were also significantly larger than those seen in TC_B (Figure 6C), with the largest differences being at the plough (Ile164: TC_A, 30 Hz; TC_B, 17 Hz), near the catalytic site (Ile488: TC_A, 22 Hz; TC_B, 10 Hz), and at the CTD (Ile641: TC_A, 58 Hz; TC_B, 32 Hz). This suggests that TC_A, the correct initiation complex, was both structurally and dynamically distinct from the nonphysiological TC_B.

Table 5: k_{ex} Values of P2 in Two Stable Initiation Complexes[a]

state	Ile37	Ile96	Ile164	Ile258	Ile449	Ile488	Ile500	Ile563
TC_A[b]	1811 ± 522	ND	ND	ND	381 ± 95[c]	671 ± 145	972 ± 186	ND
TC_B[d]	1166 ± 130	2273 ± 372	ND	ND	ND	X	1411 ± 326	ND

[a]Data for Ile641 are not shown because the quality of the data for the two ternary complexes did not allow quantitative estimation of the k_{ex} values. [b]TC_A is the ternary complex formed by P2, GMPCPP, and template C1 (5′-UUU**CC**-3′) (see Figure 6A). Data for TC_A taken from ref *19*. [c]Data for Ile449 in TC_A were refitted excluding two points with large errors. The k_{ex} value obtained was unaltered within confidence bounds from that obtained previously (*19*). [d]TC_B is the ternary complex formed by P2, AMPCPP, and template C5 (5′-UUU**UU**-3′) (see Figure 6B).

CONCLUSIONS

From this analysis, it appears that different RNA templates affect dynamics on the slow time scale in P2 in a fashion that is not correlated with their relative affinities in a straightforward way. ssRNA templates corresponding to the proper genomic 3′-ends have similar effects on structure and dynamics that are distinct from higher-affinity nongenomic RNA constructs. The effects of substrates ATP (AMPCPP) and GTP (GMPCPP), the latter being the correct initiation nucleotide, on dynamics are also distinct.

In the presence of AMPCPP or the nonphysiological ssRNA (C5), the motion of Ile641 moves to a slower time scale, decoupling the motion of the CTD from that of the template portal, likely disrupting the coordinated motion of the template into and the daughter chain out of the catalytic pore (*4*, *19*). In nonphysiological ternary complex TC_B, residues around the catalytic site also do not show dynamics on the catalytic time scale as in the proper initiation complex, TC_A. Additionally in TC_A, motions of motif C bearing the conserved catalytic Asp residues (reported by Ile449) on the catalytic time scale become activated.

The case of motif E residue Ile500 is most intriguing. In all of the complexes with template RNA in the absence of substrate, motion of this residue is fast, on the group I time scale. However, in the presence of the correct initiation NTP (GTP), even in the absence of template, this motion switches to a catalytic time scale (group II) that persists in physiological complex TC_A. This residue is spatially proximal to Glu491 and Ala495 that are shown to coordinate a structural Mn^{2+} (*4*, *9*, *10*). Mutation of Glu491 results in a polymerase that has an altered thermal stability and crystallizes in two forms, one of which has a modified catalytic site geometry, suggesting significant conformational dynamics (*9*). This mutant is also compromised both in the formation of the initiation complex and in chain elongation. This suggests its influence on both catalysis and RNA translocation, i.e., on both group I and II motions. It is therefore likely that motif E needs to sample both group I- and group II-type motions depending on the stage of the catalytic cycle. Thus, we would expect that group II time scale motions would be activated in this region in the presence of the correct substrate and subsequently upon formation of the proper initiation complex and commencement of catalysis. This hypothesis is in line with our data. The group II time scale motions of Ile164 were damped in the presence of both AMPCPP and GMPCPP, and no motions were activated for this residue in either of the ternary complexes. The role of the plough region (reported by Ile164) in catalysis has been documented (*11*). From these results, it seems that bound substrate molecules have to be present to damp the motion of the plough, but this damping does not depend on the precise nature of the substrate. Additionally, group II motions involving Ile258 (except for C5) and Ile563 were completely suppressed in the presence of all ligands we studied. The role of the motions reported by these residues, Ile258 that lies extreme end of the fingers domain and Ile563 that lies at the base of the thumb domain, is not immediately clear. Further studies are required to ascertain the role of these regions, if any, in catalysis.

The results of this study combined with those of our previous one (*19*) reflect a network of fast (group I) and slow (group II) dynamic modes, broadly classified, on the microsecond to millisecond time scale involving several regions of the protein. We also find that recognition of the correct genomic 3′-ends, the proper initiation NTP substrate (GTP), to form the correct initiation complex activates distinct changes in the structure and dynamics of ϕ6 P2 to initiate RNA synthesis. On the other hand, nonoptimal NTP substrates or nonphysiological templates, despite having a higher affinity for P2, fail to elucidate these changes.

As described previously (*19*), it is highly plausible that group I and group II motions could have an additional hierarchy of time scales within them as implied by the broad time scale range in our simple classification. Multistep processes, with multiple rates, have been used in the analysis of the catalytic process for the homologous 3Dpol [as described previously (*12*)]. The presence of this hierarchy becomes clear in attempting to perform global fits on the residues within the group I and II classification. For example, for the reference state, residues Ile37, Ile96, and Ile500, all classified as group I residues (Tables 3 and 4), can be fit in a statistically significant way to a common k_{ex} value of ~1400 s^{-1}. Also for the reference state, Ile164, Ile258, and Ile563, all classified as group II residues (Tables 3 and 4), can also be fit to a common k_{ex} value of ~350 s^{-1}. However, inclusion of Ile488, also classified as a group II residue in this global fit, leads to a common k_{ex} of ~450 s^{-1} with a substantial increase in the residual variance, and the global fit can no longer be considered to be statistically significant. This hints toward a common origin for motions involving Ile164, Ile258, and Ile563 and a distinct one for Ile488, within the group II time scale. However, a detailed interpretation of this hierarchy is not possible at the level of precision, both theoretical and experimental, of our experiments. Global fitting also provides some insight into the time scale switching as shown by the residue Ile500, for example. This residue that could be fitted using the group I time scale, together with Ile37 and Ile96 (as described above) using a common k_{ex} value of 1400 s^{-1} for the reference state, can be fit with a common k_{ex} value of 750 s^{-1} with Ile488 in the GMPCPP-bound state (Table 4). Additional experiments at multiple fields coupled

with single-quantum dispersion measurements[2] should allow the determination of the underlying substructure of the motional modes broadly classified as group I and group II time scales. Further, a definitive picture of the influence of motion in residue-by-residue detail also awaits the availability of complete or near-complete assignment of backbone resonances. However, for a system as large as P2 coupled with the difficulty in solubilizing it at the high concentrations required for standard triple-resonance experiments used for backbone-directed assignment strategies, this is an extremely slow and tedious process. The almost uniform distribution of the 25 Ile residues over the structural domains and most of the conserved polymerase sequence motifs, together with the ease in labeling of the Ile $\delta 1$ position (*27*), and the excellent spectral dispersion afforded by the corresponding resonances (see Figure 4), makes these residues excellent probes for analyzing large-scale dynamics and obtaining insight into the finely tuned molecular machine that is P2, while awaiting backbone resonance assignments. As recently suggested by Cameron (*14*), it is becoming more and more obvious that dynamics certainly seems to be the missing link between structure and function in polymerase based on our present and earlier (*19*) results, and those from the elegant study of 3Dpol (*17*). Measurement and interpretation of NMR relaxation are likely to play a pivotal role in fully elucidating this connection. However, it should be remembered that mere overlap of dynamic time scales measured by NMR with catalytic time scales does not necessarily prove causality. These studies have to be coupled with rational mutations that affect the dynamics as measured by NMR and also have an influence on catalytic rates and time scales measured from kinetic analyses to definitively establish their correlation.

ACKNOWLEDGMENT

We thank Drs. Lewis Kay and Dimitri Korzhnev (University of Toronto, Toronto, ON) for the pulse sequences used in measuring multiple-quantum relaxation rates, Dr. Hsin Wang (The City College of New York) for help with NMR spectroscopy, and Dr. Aneel Aggarwal (Mt. Sinai School of Medicine, New York, NY) for use of the Beacon spectrofluorometer. We are grateful to Dr. Leonard Mindich (Public Health Research Institute, Newark, NJ), Dr. Andrea Piserchio (The City College of New York), and Dr. Kaushik Dutta (New York Structural Biology Center, New York, NY) for useful comments and suggestions.

REFERENCES

1. Poranen, M. M., and Tuma, R. (2004) Self-assembly of double-stranded RNA bacteriophages. *Virus Res. 101*, 93–100.
2. Ferrer-Orta, C., Arias, A., Escarmis, C., and Verdaguer, N. (2006) A comparison of viral RNA-dependent RNA polymerases. *Curr. Opin. Struct. Biol. 16*, 27–34.
3. Bruenn, J. A. (2003) A structural and primary sequence comparison of the viral RNA-dependent RNA polymerases. *Nucleic Acids Res. 31*, 1821–1829.
4. Butcher, S. J., Grimes, J. M., Makeyev, E. V., Bamford, D. H., and Stuart, D. I. (2001) A mechanism for initiating RNA-dependent RNA polymerization. *Nature 410*, 235–240.
5. Makeyev, E. V., and Bamford, D. H. (2000) Replicase activity of purified recombinant protein P2 of double-stranded RNA bacteriophage $\phi 6$. *EMBO J. 19*, 124–133.
6. Makeyev, E. V., and Bamford, D. H. (2000) The polymerase subunit of a dsRNA virus plays a central role in the regulation of viral RNA metabolism. *EMBO J. 19*, 6275–6284.
7. Makeyev, E. V., and Grimes, J. M. (2004) RNA-dependent RNA polymerases of dsRNA bacteriophages. *Virus Res. 101*, 45–55.
8. Yang, H., Makeyev, E. V., and Bamford, D. H. (2001) Comparison of polymerase subunits from double-stranded RNA bacteriophages. *J. Virol. 75*, 11088–11095.
9. Poranen, M. M., Salgado, P. S., Koivunen, M. R., Wright, S., Bamford, D. H., Stuart, D. I., and Grimes, J. M. (2008) Structural explanation for the role of Mn^{2+} in the activity of $\phi 6$ RNA-dependent RNA polymerase. *Nucleic Acids Res. 36*, 6633–6644.
10. Salgado, P. S., Makeyev, E. V., Butcher, S. J., Bamford, D. H., Stuart, D. I., and Grimes, J. M. (2004) The structural basis for RNA specificity and Ca^{2+} inhibition of an RNA-dependent RNA polymerase. *Structure 12*, 307–316.
11. Sarin, L. P., Poranen, M. M., Lehti, N. M., Ravantti, J. J., Koivunen, M. R., Aalto, A. P., van Dijk, A. A., Stuart, D. I., Grimes, J. M., and Bamford, D. H. (2009) Insights into the pre-initiation events of bacteriophage $\phi 6$ RNA-dependent RNA polymerase: Towards the assembly of a productive binary complex. *Nucleic Acids Res. 37*, 1182–1192
12. Arnold, J. J., and Cameron, C. E. (2004) Poliovirus RNA-dependent RNA polymerase (3Dpol): Pre-steady-state kinetic analysis of ribonucleotide incorporation in the presence of Mg^{2+}. *Biochemistry 43*, 5126–5137.
13. Castro, C., Smidansky, E. D., Arnold, J. J., Maksimchuk, K. R., Moustafa, I., Uchida, A., Gotte, M., Konigsberg, W., and Cameron, C. E. (2009) Nucleic acid polymerases use a general acid for nucleotidyl transfer. *Nat. Struct. Mol. Biol. 16*, 212–218.
14. Cameron, C. E., Moustafa, I. M., and Arnold, J. J. (2009) Dynamics: The missing link between structure and function of the viral RNA-dependent RNA polymerase? *Curr. Opin. Struct. Biol. 19*, 768–774.
15. Patel, S. S., Wong, I., and Johnson, K. A. (1991) Pre-steady-state kinetic analysis of processive DNA replication including complete characterization of an exonuclease-deficient mutant. *Biochemistry 30*, 511–525.
16. Arnold, J. J., Vignuzzi, M., Stone, J. K., Andino, R., and Cameron, C. E. (2005) Remote site control of an active site fidelity checkpoint in a viral RNA-dependent RNA polymerase. *J. Biol. Chem. 280*, 25706–25716
17. Yang, X., Welch, J. L., Arnold, J. J., and Boehr, D. D. (2010) Long-range interaction networks in the function and fidelity of poliovirus RNA-dependent RNA polymerase studied by nuclear magnetic resonance. *Biochemistry 49*, 9361–9371.
18. Di Marco, S., Volpari, C., Tomei, L., Altamura, S., Harper, S., Narjes, F., Koch, U., Rowley, M., De Francesco, R., Migliaccio, G., and Carfi, A. (2005) Interdomain communication in hepatitis C virus polymerase abolished by small molecule inhibitors bound to a novel allosteric site. *J. Biol. Chem. 280*, 29765–29770.
19. Ren, Z., Wang, H., and Ghose, R. (2010) Dynamics on multiple timescales in the RNA-directed RNA polymerase from the cystovirus $\phi 6$. *Nucleic Acids Res. 38*, 5105–5118.
20. Choi, K. H., Groarke, J. M., Young, D. C., Kuhn, R. J., Smith, J. L., Pevear, D. C., and Rossmann, M. G. (2004) The structure of the RNA-dependent RNA polymerase from bovine viral diarrhea virus establishes the role of GTP in de novo initiation. *Proc. Natl. Acad. Sci. U.S.A. 101*, 4425–4430.
21. Korzhnev, D. M., Kloiber, K., Kanelis, V., Tugarinov, V., and Kay, L. E. (2004) Probing slow dynamics in high molecular weight proteins by methyl-TROSY NMR spectroscopy: Application to a 723-residue enzyme. *J. Am. Chem. Soc. 126*, 3964–3973.
22. Mindich, L., Qiao, X., Onodera, S., Gottlieb, P., and Frilander, M. (1994) RNA structural requirements for stability and minus-strand synthesis in the dsRNA bacteriophage $\phi 6$. *Virology 202*, 258–263.
23. Boggs, P. T., Donaldson, J. R., Byrd, R. H., and Schnabel, R. B. (1989) ODRPACK software for weighted orthogonal distance regression. *ACM Trans. Math. Software 15*, 348–364.

[2]Note that unlike relaxation dispersion for single-quantum (SQ) coherences (R_2 dispersion), an exact analysis yielding interpretable $\Delta\omega_H$ and $\Delta\omega_C$ in addition to k_{ex} values cannot, in general, be obtained for MQ dispersion even if data at multiple fields are available (except perhaps if the data are highly precise, an unlikely situation in the case of a protein like P2) given the extremely complex nature (*21*) of MQ dispersion curves (compare the simplified eq 4 that is valid for only fast exchange and when the product $\Delta\omega_C\Delta\omega_H$ is small). For the complete analysis, MQ dispersion measurements need to be combined with SQ data (*21*).

24. Delaglio, F., Grzesiek, S., Vuister, G. W., Zhu, G., Pfeifer, J., and Bax, A. (1995) NMRPipe: A multidimensional spectral processing system based on UNIX pipes. *J. Biomol. NMR 6*, 277–293.
25. Dittmer, J., and Bodenhausen, G. (2004) Evidence for slow motion in proteins by multiple refocusing of heteronuclear nitrogen/proton multiple quantum coherences in NMR. *J. Am. Chem. Soc. 126*, 1314–1315.
26. van Dijk, A. A., Makeyev, E. V., and Bamford, D. H. (2004) Initiation of viral RNA-dependent RNA polymerization. *J. Gen. Virol. 85*, 1077–1093.
27. Tugarinov, V., and Kay, L. E. (2005) Methyl groups as probes of structure and dynamics in NMR studies of high-molecular-weight proteins. *ChemBioChem 6*, 1567–1577.